Subject index: *Propagation, diffraction and scattering*

X-RAY DARK-FIELD REFRACTION-CONTRAST IMAGING OF MICROOBJECTS

Vladimir V. Protopopov[a], Jaroslav Sobota[b],
[a]The Institute of Physics and Technology, Moscow, Russia;
[b]Institute of Scientific Instruments, Academy of Sciences of Czech Republic;

Corresponding author: Dr. V.V.Protopopov of the Institute of Physics and Technology, Nakhimovskii Pr. 34, Moscow, 117218, Russia, Phone: (+095)332-49-40,
Fax: (+095)129-31-41, e-mail: v.protopopov@mtu-net.ru

Abstract

An X-ray multilayer mirror, consisting of two periodical reflecting structures separated by a quarter-wave spacer, can be designed so that to have a very sharp and deep resonant absorption at a definite angle of incidence. Such a mirror may be used as an angular dispersive element for refractive X-ray radiography. In this method that can be referred to as the dark-field refraction contrast imaging the image contrast is obtained not due to variation of absorption but due to variation of the refractive index of the object inner structure. Signal-to-noise ratio in the image can be significantly enhanced, and the dynamical range of the detector can be reduced due to suppression of the shot noise produced by the direct beam. Theoretical basis for this method is developed, providing definite rules for designing of the mirror with resonant absorption, and explaining the limitations on the detector spatial resolution. Refraction contrast images of a copper wire 75 μm in diameter and a human hair were experimentally observed using Ni/C multilayer mirror with resonant absorption at CuK_α radiation (1.54Å). The multilayer structure consisting of 30 bilayers was designed for CuK_α radiation so as to have absorbing resonance of the width of about several arc seconds at a grazing angle of 0.8°. A monochromatic probe X-ray beam with a divergence of approximately 5 arc seconds was obtained from a conventional X-ray tube and a double crystal monochromator set in a strongly dispersive configuration.

PACS: 61.10.-i; 41.50. +h
Keywords: X-ray Imaging, Radiography, Refraction, Multilayers.

1. Introduction.

In the last few decades a variety of new medical imaging techniques was introduced, using almost all known wave domains: from sound waves to gamma rays, and elementary particles. However, X-ray radiography is still a dominant technique, and X-ray devices span of approximately 60% of all medical diagnostic devices. The contrast and spatial resolution of X-ray radiography became extremely important in the past decade due to the problem of medical diagnostics. Radiation dose is also a very important parameter, determining safety of the technique. Absorption contrast as the basic principle of imaging in traditional X-ray radiography remained essentially unchanged since Roentgen's first experiments a hundred years ago. Therefore, the only way to recognize small-scale features of small objects in traditional X-ray images is to increase the dose of radiation absorbed by a whole sample. It is well known, however, that this way is unacceptable in medical applications for safety reasons. Moreover, the limited dynamical range of electronic image detectors is the additional barrier on this way. The first phase shift image of a non-crystalline object was obtained, probably, by Bonse and Hart [1]. Today, it is both experimentally and theoretically proven that the refractive contrast, originating from the variation of the refractive indices of different parts of a sample, produces far more detailed images of biological tissues, and a variety of imaging techniques for biological and medical investigations based on refraction contrast are being developed using both the laboratory X-ray sources and coherent synchrotron radiation sources [2-6].

In all of these techniques, sometimes referred to as phase-contrast imaging, the commonly weak useful signal is detected against the background of a strong direct beam. Therefore, the detector shot noise produced by the direct beam decreases the signal-to-noise ratio, which is of a primary importance when an image is recorded electronically. Recently, a new scheme of X-ray refractive radiography was proposed, that can significantly suppress the intensity of a direct beam [7,8] and enhance the signal-to-noise ratio. In this scheme a specially designed multilayer mirror with resonant absorption plays the role of the angular analyzer. In the present paper we explain the physical idea of X-ray multilayer mirrors with resonant absorption and outline the technology for manufacturing it, discuss the influence of spatial resolution of a detector and the results of numerical simulation, and finally present the experimental results obtained with microobjects, including 2D images of human hairs.

2. Idea of the method.

The idea of the X-ray refractive radiography is schematically shown in Fig.1. A parallel X-ray beam with a wave vector $\mathbf{k}_0$ penetrates the object, transparent to X rays. Because of the refraction of X rays on the inner structure of the object, the output beam is composed of the original wave with the vector $\mathbf{k}_0$ and the refracted waves with vectors $\mathbf{k}(\Delta\theta)$ slightly declined from the initial vector $\mathbf{k}_0$. The key part of the scheme is the analyzer, which differentiates the output waves

by their direction $\Delta\theta$. In all the schemes used before the role of the analyzer is played by a highly perfect crystal with transmission characteristics in the form of a step function (Fig.2), working in a very narrow angular interval of about a few arc seconds. In order to be sensitive to both directions of the refraction, the working point is usually chosen in the position marked as number 1 in Fig.2. Of course, it is possible to choose any other position as the working point, for instance, 2 or 3, but that will lead to a loss of useful beam energy. Thus, the resultant image registered directly behind the analyzer is formed by the intensity variations $R(\theta)$ proportional to the angle of refraction $\Delta\theta$. Therefore, the resultant intensity distribution in the image plane may be presented in the form of a sum

$$I(\mathbf{r}) = R[\theta(\mathbf{r})] + I_0 , \qquad (1)$$

where I_0 is the intensity of the direct beam, which may be much greater than the useful term $R[\theta(\mathbf{r})]$. The direct beam carries practically no information about the object, if the latter is transparent to X rays, and at the same time it deteriorates the image, bringing additional noise into it. For these reasons, the direct beam is undesirable.

Suppose now, that the crystal analyzer with the angular characteristic shown in Fig.2 is replaced by a multilayer mirror with the reflection curve shown in Fig.3 in a generalized form. Evidently, the intensity of a direct beam I_0 in this case may be much less, than in the previous case, while the sensitivity of the scheme with respect to the refracted beams is determined by the sharpness of the reflection curve around the resonant angle θ_r. Note that unlike a crystal analyzer, the multilayer analyzer produces symmetrical output for the refracted beams with both positive and negative values of $\Delta\theta$.

3. Physics of multilayer mirrors with resonant absorption.

Physics of a multilayer mirror with resonant absorption is the same as that of the Fabri-Perrot interferometer. It can be represented as two periodical multilayer mirrors separated by quarter-wave spacer made of weakly absorbing material (Fig.4). Consider a plane wave, coming to the multilayer structure at the grazing angle θ. The kinematical theory assumes that the refraction effects and the attenuation due to both reflection at the interfaces and photoabsorption are negligible. When the multilayer structure is designed for maximum peak reflectivity one can consider the two systems of waves, reflected from different interfaces in one bilayer, as one system of waves reflected from planes separated from each other by a gap equal to the bilayer thickness that is the period of the structure. Suppose initially that the two multilayer structures have different periods d_1 and d_2, corresponding to first Bragg reflections at the angles θ_1 and θ_2 respectively. Then the straightforward idea of how to obtain a narrow absorbing dip in such a multilayer structure can be

easily understood from Fig.5. It is necessary only to introduce a phase shift equal to π between the waves reflected from both reflecting structures. Then amplitudes will act in counterphase, and the resultant intensity will be equal to zero at the angle between θ_1 and θ_2. The complex amplitude of the reflected wave can be written as

$$E_r = E_0\,\rho\sum_{n=1}^{N}\exp(ik2d_1 n\sin\theta)+E_0\,\rho\cdot e^{i\varphi}\cdot\sum_{n=1}^{N}\exp(ik2d_2 n\sin\theta);$$
$$\varphi = k\,2(d_1 N + d_s)\sin\theta\,. \qquad (2)$$

Here E_0 is the complex amplitude of the coming wave, ρ is the Fresnel complex reflection coefficient at the interfaces, d_s is the thickness of the spacer, and k is the wave number. For the sake of conciseness of mathematical transformations we took the number of periods N the same for the both reflecting structures, and E_0 can be put equal to unity. The sums in (2) can be easily calculated using the formula for the geometrical sequence, so that the intensity $I = |E_r|^2$ can be presented in the following form:

$$I = r^2(\theta-\theta_1)+r^2(\theta-\theta_2)+2r(\theta-\theta_1)r(\theta-\theta_2)\cdot\cos\psi(\theta);$$
$$r(\theta)=\rho\frac{\sin(kNd\sin\theta)}{\sin(kd\sin\theta)};\quad \psi(\theta)=2k(Nd+d_s)\sin\theta\,; \qquad (3)$$
$$d=(d_1+d_2)/2\,.$$

Strictly speaking, functions r corresponding to different Bragg angles differ from each other because of different d. However, this difference is relatively small and will not affect the main result.

We shall define the resonant angle as

$$\theta_r = \frac{\theta_1+\theta_2}{2}\,. \qquad (4)$$

Then $r(\theta_r-\theta_1)=r(\theta_r-\theta_2)$, and the intensity at the resonant angle will be zero if $\cos\psi(\theta_r)=-1$, i.e., when

$$\psi(\theta_r)=\pi+2\pi m,\quad m=0,1,2,\ldots\,. \qquad (5)$$

Thus, the condition for resonance is as follows:

$$d_s = \frac{2\pi m+\pi}{2k\theta_r} - Nd\,. \qquad (6)$$

The sharpness of the resonance is the most important parameter in those cases when a multilayer mirror is used as an angular analyzer. Therefore, it is interesting to investigate the intensity of the reflected wave as a function of the angular deviation from the resonance $\theta-\theta_r=u$.

Making use of small values of both the θ_r and θ , that are of the order of 1 degree for hard X rays, one can obtain from (3) assuming $N >> 1$:

$$r(\theta) \approx \rho N\left[1-\frac{1}{6}\left(kN^2 d\theta\right)^2\right], \tag{7}$$

and assuming $d_s >> d$, $Nd >> d_s$:

$$I(u) \approx (2\rho kLN\, u)^2\left[1-\frac{1}{18}(\theta_1-\theta_2)^2(kdN)^2\right], \tag{8}$$

where $L = Nd + d_s$ is the total thickness of the structure. The first conclusion that can be drawn from (8) is that the resonant minimum is a quadratic function of the angular deviation. The second thing is that the sharpness reaches its maximum value when $\theta_1 = \theta_2$, i.e., when the two periodical multilayer structures have the same period. Behavior of $I(u)$ according to (3) is illustrated in Fig.6 for the two cases of equal and different θ_1 and θ_2 . Now we can address again our initial physical idea sketched in Fig.5. In terms of formulas (3) it corresponds to the situation when $I(u)$ is the full quadrate, i.e., when $\cos\psi = -1$ for all grazing angles θ . A curve representing this case is shown in Fig.6 as the curve (c). Evidently, the actual functions (a) and (b) are far more sharp because their amplitudes are produced by coherent interference of the waves reflected from the upper and lower periodical multilayer structures, and not by adding only the intensities of these waves, as was assumed in our initial idea. If an extremely thick spacer $d_s > Nd$ is introduced between reflecting structures then a large number of extremely sharp resonant dips is observed inside the reflecting peak. This situation will be discussed at the end of this section.

In terms of kinematical theory the peak reflection coefficient of the multilayer structure without the spacer is equal to $R_0 = \rho^2 (2N)^2$ .Therefore, the angular dependence of the coefficient of reflection according to (8) may be rewritten in a more general form:

$$R(\theta) = R_0 \cdot [kL(\theta - \theta_r)]^2 . \tag{9}$$

From this formula it follows that the larger is the total thickness of the multilayer structure the sharper is the resonant dip. This analytical conclusion is consistent with the results of rigorous computations presented below in this section. Note that the dependence of the sharpness on the wavelength is not so straightforward, because not only the wave number k depends on the wavelength, but also the Fresnel reflection coefficient ρ . Moreover, the kinematical model takes into account nor the photoabsorption not the attenuation due to reflection that is crucial in practice. This problem will be discussed briefly below in this section on the basis of numerical computations.

Designing the mirror for X-ray imaging, it is important to understand how to properly choose the value of the resonant angle. In many cases the thickness of the spacer is not very large, so that

$L \approx dN$. Then, taking into account the Bragg formula for d, it is possible to rewrite (9) in the following form:

$$R(\theta) \approx R_0 \left(\pi N \frac{\theta - \theta_r}{\theta_r} \right)^2 . \qquad (10)$$

Here R_0 also depends on θ through the Fresnel reflection coefficient ρ , that rapidly falls with growing θ . Thus, the smaller is the resonant angle the larger is the sharpness of the resonant dip.

Consider now the results of rigorous numerical calculations. There is no need in describing the specific mathematical routine for that, because innumerous variety of routines is known to day, based on the Parratt recursive procedure [9]. We used the optimization procedure for designing X-ray multilayer mirrors with resonant absorption supplied with the ProtoSoftware package. This software provides calculation of the optimal spacer thickness and its optimal positioning inside the periodical multilayer structure. According to (9) the larger the spacer thickness the sharper is the dip. However, in practice the thickness of the spacer is limited by technological considerations, such as, for example, the growth of roughness. Therefore, we limited the maximum thickness of the spacer by the value of 400Å. Typical calculated reflection curve is shown in Fig.7.

In order to compare different designs it is necessary to introduce a parameter that describes the sharpness of the resonant dip. According to (9) the appropriate constant is $v = (1/2)\left(d^2R/d\theta^2\right)_{\theta=\theta_r}$. The results of numerical calculations for various number of layers are summarized in the Table 1. The sharpness for MoK radiation grows more rapidly with the number of layers relative to the case of CuK radiation because penetrating ability of MoK radiation is higher, and, therefore, the larger number of layers works efficiently. The results of numerical calculations for various resonant angles are summarized in the Table 2. The lower values of v for MoK radiation are obtained due to lower Fresnel reflection coefficients at the interfaces. However, it does not mean that the sharpness at MoK radiation is always worse, because due to lower absorption it is possible to obtain larger effective thickness of the structure with the larger number of periods and thicker spacer.

It is worth also to examine briefly the case of very large spacer thickness, when $d_s > Nd$. Then the phase $\psi(\theta)$ in (3) varies more rapidly with θ relatively to the argument of $r(\theta)$, and, therefore, the condition for resonance (5) occurs many times inside the main peak of $r(\theta)$. It means that not a single resonant dip will be observed inside the first Bragg maximum of $r(\theta)$, but a series of extremely sharp dips as it is shown in Fig.8.

4. Refraction contrast and the spatial resolution of the detector.

In this section we shall both theoretically and with the help of numerical simulation examine how the spatial resolution of the detector diminishes the amplitude of the refraction contrast signal.

Consider cylindrical object (a fiber) with a radius r in its cross section (Fig.9). At the boundary the Snellius law gives:

$$(1-n)\sin\alpha' = \sin\alpha\,, \tag{11}$$

where n is a small quantity of the order of $10^{-4}\div10^{-6}$, describing the refractive index of a fiber in the X-ray domain. According to (11), when $\alpha' = \pi/2$ the total external reflection takes place. Therefore, (11) holds true when

$$\sin\alpha \le 1-n, \quad \text{or} \quad \alpha \le \frac{\pi}{2} - \sqrt{2n}\,. \tag{12}$$

From (11) it follows that small deviation from the original direction of the beam inside the object is equal to

$$\delta\alpha = n\tan\alpha\,, \tag{13}$$

and the total deviation of the exiting beam equals approximately twice that value.

It follows from the previous section that the reflection curve of the mirror can be written approximately as a quadratical function of $\delta\alpha$:

$$R(\delta\alpha) = v\cdot(\delta\alpha)^2\,, \tag{14}$$

where v is a constant. Thus, the intensity behind the mirror is equal to

$$I(\alpha) = I_0\,R(\delta\alpha) = 4I_0 v\,(n\tan\alpha)^2\,. \tag{15}$$

Useful power gathered from the element ds and transferred to a detector signal is equal to

$$dP = I(\alpha)ds = 4I_0 v\cdot(n\tan\alpha)^2\cdot r\,d\alpha\cos\alpha = 4I_0 v\,rn^2\cdot\frac{\sin^2\alpha}{\cos\alpha}d\alpha\,. \tag{16}$$

Total useful power behind the mirror must be obtained by integration of (16) over $d\alpha$ in the limits [0; $\pi/2-\sqrt{2n}$]:

$$P = 4I_0 v\,rn^2\int_0^{\pi/2-\sqrt{2n}}\frac{\sin^2\alpha}{\cos\alpha}\,d\alpha\,. \tag{17}$$

This integral diverges at the upper limit. In Appendix it is shown that

$$\int_0^{\pi/2-\varepsilon}\frac{\sin^2(\alpha)}{\cos(\alpha)}d\alpha = -0.3068-\ln(\varepsilon);\quad \varepsilon<<1. \tag{18}$$

Therefore,

$$P \approx 2I_0 v\,rn^2\left|\ln n\right|\,. \tag{19}$$

Thus, that total power registered in the dark-field mode is proportional to fiber's radius, and in a finite interval of values of the refraction index rises faster than quadratically with the refraction index.

The expression for the intensity behind the mirror as a function of the transversal coordinate can be obtained from (15), taking into consideration that $\sin\alpha = x/r$:

$$I(x) = 4I_0 \nu n^2 \frac{x^2}{r^2 - x^2}; \quad |x| \le (1-n)r \ . \tag{20}$$

This simple formula is graphically shown in Fig.10. It can be compared to the results of careful numerical simulation that takes into account the real resonant reflection curve obtained in the experiments as described in the next sections. The results of numerical simulation are presented in Fig.11. Theoretical distribution as given by (20) is qualitatively consistent with the numerical results with the exception, of course, for the bottoms of the curves which are below the average level due to absorption. The peak intensity, according to (20), is proportional to n :

$$\{I(x)\}_{\max} = 2I_0 \nu n \ . \tag{21}$$

However, in practice intensity distribution is always measured by a detector that has finite spatial resolution. Therefore, the experimentally measured intensity will depend not only on the optical constant of the object's material, but on the detector's spatial resolution as well. Consider the influence of a spatial resolution in more details.

Suppose spatial resolution of the detector is equal to Δx as it is shown in Fig.12. Parameter a is a random variable uniformly distributed in the interval [0, Δx]. Therefore, its average value is equal to

$$\frac{1}{\Delta x}\int_0^{\Delta x} a\, da = \frac{\Delta x}{2} . \tag{22}$$

The detector maximum amplitude is then proportional to the integral over a single sensitive element:

$$A = 4I_0 \nu n \cdot \frac{1}{\Delta x}\int_{(1-n)r-\Delta x/2}^{(1-n)r} \frac{x^2}{r^2 - x^2}\, dx \ . \tag{23}$$

Compare the values of the parameters in this formula. For example, for β-keratine, the main component of a human hair, n =7·10^{-6}. For carbon n =7.3·10^{-6}. The spatial resolution of the detector can hardly be better than 1 μm. Therefore, for the object's feature of any reasonable dimensions the product nr is far less than any attainable resolution of a detector. In this case the formula (23) can be transformed to a simpler form (see Appendix):

$$A = I_0 \nu \left(\frac{2nr}{\Delta x}\right) \ln\frac{\Delta x}{2nr}; \quad \Delta x >> nr \ . \tag{24}$$

From (24) it follows that maximum amplitude is a function of a single dimensionless parameter $2nr/\Delta x$, and rises with it less fast than directly proportionally. Two main conclusions can be drawn from this formula. The first thing is that low spatial resolution, i.e., large Δx , leads to low detector signal. And the second is that the larger the diameter of an object the larger is the signal. In order to estimate quantitatively the practically tolerable value of spatial resolution we shall address the results

of numerical simulation presented in Fig.13 for the case of a human hair of 50 μm in diameter. From these data it can be concluded that the spatial resolution must be better than 10 μm for this type of objects.

5. Numerical simulation of the dark-field imaging.

The possible advantage of the dark-field refraction contrast imaging with respect to the traditional absorption radiography can be estimated by means of 3D numerical simulation according to the simplified model shown in Fig.14. The case when the image is recorded in the plane P_1 corresponds to traditional absorption radiography, and the case with the image registration in the plane P_2 – to the dark-field refraction contrast imaging. Consider an object in a form of a small ball of 50 μm in diameter immersed in water. Angular dispersion of the mirror is determined by the reflection curve shown in Fig.7. The particular numerical values of the resonant dip correspond to the real Ni/C mirror that will be discussed below in the section 6.1. The results are presented in Fig.15. Left column corresponds to absorption radiography, right – to the dark-field refraction contrast imaging. For heavy materials with strong absorption, such as tungsten, both of these methods give good contrast. But the materials with low absorption, such as carbon, or beta-keratin (protein, the basic component of a human hair), are practically transparent at the wavelength of 1.54Å. Therefore, small objects made of these materials, such as, for example, a ball of 50 μm in diameter, produce practically no absorption contrast. Nevertheless, they can be detected, and their shape can be easily recognized by the dark-field refraction contrast method, as it is clear from the right column in Fig.15.

6. Experimental results.

6.1. Multilayer mirror with resonant absorption.

We have successfully overcome all technological problems and created Ni/C multilayer mirror with resonant absorption using magnetron sputtering installation LEYBOLD Z550. The mirror structure was designed for the wavelength 1.54Å with the help of the optimization routine from the software package ProtoSoftware so as to have the resonance at the grazing angle 0.8°. Multilayer coating consisting of 30 bilayers was deposited on flat quartz substrate 40×40 mm^2 with average roughness 6Å and surface shape variation not more than 3 arc seconds. Carefully balanced magnetron sputtering equipment produces random variations of the average layers thickness as small as 0.1÷0.5Å [10]. Sputtering unit Z 550 was equipped with two 150 mm cathodes of nickel and carbon. The cathodes were in side-by-side configuration as shown in Fig. 16. Multilayer structure was deposited in radio frequency mode (13.56 MHz), and the distances of the 48mm between the targets and the rotating substrate holder were held constant. The deposition rates were evaluated from the film thickness using Talystep profilometer. Argon was introduced into chamber and

regulated by HI-TEC mass -flow controller (F-100) with the reproducibility of 0.2%. The total sputtering pressure measured with MKS A270B was approximately 0.2 Pa. The computer software was developed to keep argon pressure constant and to vary the flow of argon. For the deposition of the multilayer X-ray mirrors with resonant absorption the lateral fractional variation of the thickness inside the working area must be very small (less than 0.2%) and thus the whole deposition system (i.e. gas pressure, radio-frequency power, rotation speed etc..), must be stable within a tenth of a percent. Practical experiments on our equipment show that such stability is, at least during the time of the deposition, obtainable.

Reflection curve of the mirror measured in the angular region around the resonance is presented in Fig.17. It is very similar to the theoretical curve shown in Fig.7 that proves that the deposition process was close to optimal. However, this figure presents laterally averaged value of the reflection, and does not show the lateral variation of the resonant angle. It may be that local resonances are even sharper and deeper than that shown in Fig.17. This question was investigated according to the scheme sketched in Fig.18. Linear detector array investigates the lateral variation of the reflection coefficient along x axis on the mirror's surface, while rotation around ω axis enables to view this variation as a function of different grazing angles θ. Thus, it is possible to obtain a 2D map in the coordinates ω-x. We called this technique "ω-x mapping". The result obtained with the probe beam divergence equal to 5 arc seconds is shown in Fig.19. Vertical tilt of the picture in Fig.19a is due to lateral shift of the beam along the detector during angular scanning. The two "hills" correspond to the peaks of the reflection curve separated by the "valley", that is the resonant dip itself. In the case of an ideally uniform structure the picture must not depend on the x coordinate. However, we see that, firstly, the "hills" are rounded at both sides of the mirror, and, secondly, the "valley" has the shape of an arc. A possible reason for these effects is the curvature of the mirror's surface. Before depositing multilayer coating we tested the substrate on flatness, and it had not more than 1 Newton fringe at λ=0.53mkm. Therefore, maximum deviation of the angle of incidence is of the order of λ/(length of mirror side) ≈ 3 arc seconds, while the width of the resonant dip itself is of the order of few arc seconds also. From this it follows that the flatness of the substrates must be far better than 1 Newton fringe. From Fig.19a it also follows that the local dip width is several times narrower than the average width seen in Fig.17. Therefore, we can obtain sufficiently better result without changing the deposition technology if only we use substrates with better flatness. Thus, manufacturing of multilayer mirrors with sufficiently deep and narrow resonant dips in the angular reflection curve is practically feasible.

6.2. Parallel and monochromatic probe X-ray beam

Estimations made in our previous paper [7] show that the divergence of the probe beam must not exceed 10 arc seconds. Apart of the divergence, the spectral width of the probe beam also plays a

significant role because the mirror's resonant angle depends on the wavelength. The natural relative spectral width of the CuK_α doublet including side wings is of the order of $4 \cdot 10^{-3}$. Calculations show that such spectral widening increases the angular width of the mirror's resonance by a value of approximately 10 arc seconds. Therefore, the probe beam must have not only extremely small divergence, but good spectral purity as well. We have created the necessary probe beam using a standard 1.5 kW X-ray tube with a copper anode and long fine focus coupled with a double crystal monochromator working in a strongly dispersive mode with both Si (111) reflections. The tube was installed in a point projection mode so as to form a point-like X-ray source with visible dimensions 0.8×0.4 mm^2. In this configuration, the horizontal divergence of the probe beam is equal to 7.4 arc seconds [11], while the relative spectral width is approximately $5 \cdot 10^{-4}$, i.e., an order of magnitude less than the natural spectral width of the CuK_α radiation. Thus, the effect of spectral widening can be neglected. The vertical divergence of the probe beam was of the order of several degrees.

6.3. 1D dark-field images of microobjects.

The scheme of the experiment is shown in Fig.20. The refracted (and, therefore, deflected from their original direction) components of the probe beam passed through the object placed immediately after the monochromator were efficiently reflected by a multilayer mirror positioned at a resonant grazing angle of 0.8° with respect to the probe beam, while the direct component was strongly attenuated. The output intensity distribution was measured in the mirror's plane of incidence by a linear detector array composed of 2580 reverse biased silicon photodiodes with individual amplifiers. Each sensitive element has the dimensions of 1×0.01 mm^2, and the spacing between the elements is equal to 2.5 μm. Thus, the geometrical spatial resolution of the detector is 12.5 μm, while its real resolution, taking into account the cross-talk between the neighboring sensitive elements, is about 20 μm. The sensitive array is assembled on a silicon substrate which is cooled and stabilized to a temperature of approximately 5C° with a Peltier refrigerator. The dark current and gain differences between single photodiodes are compensated for by taking into account the reference values measured and stored beforehand in the computer memory.

The signal-to-noise ratio was the crucial issue in the experiment. The inner noise of the detector has two components: variations of the average current drain from different sensitive elements and shot noise. The first component can be compensated for by subtracting the average output noise signal stored in the computer before measurements from the real-time signal. The second one can be reduced by averaging the output signal over both time and the number of realizations. The averaging time interval was limited by the charge leakage current, and in the experiment could not exceed 1 second. Additional averaging over 100 realizations was applied, so that the total duration of one measuring cycle was 100 seconds.

Two types of objects were used in the experiment: a copper wire 75 μm in diameter and a human hair approximately 60 μm in diameter. The experimental results obtained with a copper wire are presented in Fig.21. The central dip emerges due to absorption, while two side peaks of the opposite sign marked by the arrows arise due to refraction. In order to prove that the marked regions really correspond to a refraction contrast we removed the multilayer mirror from the probe beam, thus leaving the optical path to the detector free (Fig.21b). One can distinctly see the absence of side reflexes in this case. This mode of operation corresponds to traditional absorption radiography.

A human hair is a far less absorbing object with respect to a copper wire at CuK_α radiation. Therefore, as can be seen from Fig.22a, the central dip, originating from absorption contrast, cannot be recognized on the background of the detector shot noise. Thus, the detector couldn't identify the presence of this hair on the background of its noise if it worked in the absorption-contrast mode. However, in the dark-field refraction-contrast mode the two side peaks are clearly seen. A different type of human hair is shown in Fig.22b. Here the absorption dip is larger than in the previous case, though it is still far less than the refraction contrast peaks. Supposedly this situation corresponds to a stronger absorption of X rays in the material of the hair due to the presence of heavy elements. Thus, even such simple experimental arrangement as described above can give interesting analytical information.

6.4. 2D dark-field images of a human hair.

Finally, we present the initial results of dark-field imaging of microobjects. Fig.23 presents the images of a human hair recorded with traditional photo plates. Fig.23a corresponds to the case when the probe beam is rigorously adjusted to the resonant dip, i.e., when the grazing angle of the input beam is equal to the resonant grazing angle of the mirror. In this case both the left and right sides of the hair image are approximately equally dark. Fig.23b corresponds to another case when the probe beam is slightly tilted with respect to the resonant grazing angle of the mirror. Therefore, one side of the hair image is darker than the other, and a white strip, corresponding to those refracted rays that come to the mirror at grazing angles equal to the resonant angle, emerges at one side of the image. This type of the image resembles conventional images in visible rays when the light is coming from one side. It may be referred to as a shadow effect.

Fig.23c presents traditional absorption contrast X-ray image of the same object. With respect to the results of numerical simulation shown in Fig.15 here it is still possible to recognize the object because it was not immersed in water. Therefore, the absorption difference is high enough to produce recognizable contrast in the image. However, the width of the hair can hardly be estimated from this image.

7. Conclusions.

To day there are known three essentially different methods for refraction-contrast X-ray imiaging: the method based on sharp angular response of crystal analyzers for selecting the refracted waves, the method that uses the coherence property of the probe X-ray beam, and the so called dark field method proposed in our earlier work [7], that uses resonantly absorbing multilayer mirrors for simulataneous selection of the refracted waves and suppression of the direct beam. While the first two methods already were experimentally proven to be viable, the dark filed method had not been experimentally validated so far, and there was no clear understanding of the physical mechanism for resonant absorption in X-ray multilayer mirrors. Present paper forms theoretical basis for the X-ray dark field method of imaging, and shows its practical feasibility for laboratory-based applications.

8. Acknowledgments.

The authors are grateful to Dr. A.A. Lomov and to Prof. R.M. Imamov from the Institute of Crystallography, Russian Academy of Sciences, for their generous help and support of this work, and to Z.Bochnicek from Masaryk University, Brno, Czech Republic, for his assistance in X-ray measurements.

References

1. U. Bonse, M. Hart, Appl. Phys. Lett. **7** (1965) 99.
2. V.A. Somenkov, A.K. Tkalich, and S.S. Shilstein, J. Tech. Phys. **61** (1991) 197.
3. V.N. Ingal, and E.A. Beliaevskaya, J. Phys. D: Appl. Phys. **28** (1997) 2314.
4. V.N.Ingal E.A. and Beliaevskaya, http://www.xraysite.com/knowbase/phaseradiology.html.
5. K.A. Nugent, T.E. Gureyev, D.F. Cookson, D. Paganin, Z. Barnea, Phys. Rev. Lett. **77** (1996) 2961.
6. S.DiFonzo, W.Jark, G.Soullie, A.Gedola, S.Lagomarsin, P.Cloetans, C.Rickel, Journ. Synchrotron Radiat. 5, Pt.3 (1998) 376.
7. V.V. Protopopov, Opt. Commun. **174** (2000) 13.
8. V.V. Protopopov, V.A. Kalnov, Opt. Commun. **184** (2000) 1.
9. L.G. Parratt, Phys. Rev. **95** (1954) 359.
10. V.V.Protopopov, V.A.Kalnov, Opt. Commun. **158** (1998) 127.
11. R.Caciuffo, S.Melone, F.Rustichelli, and A.Boeuf, Phys. Rep. **152** (1987) 1.

Appendix. Calculation of the integrals (18) and (23).

Integral

$$I(\varepsilon)=\int_0^{\pi/2-\varepsilon}\frac{\sin^2(\alpha)}{\cos(\alpha)}d\alpha \tag{A1}$$

diverges with $\varepsilon\to 0$ due to $\cos\alpha$. The task is to evaluate analytically the function $I(\varepsilon)$ for small ε . It can be done by presenting the integrated function as a sum of three easily integrated functions:

$$\frac{\sin^2(\alpha)}{\cos(\alpha)}=\frac{1-\sin\alpha}{\cos\alpha}-\cos\alpha+\frac{\sin\alpha}{\cos\alpha}\ . \tag{A2}$$

Then

$$I(\varepsilon)=\int_0^{\pi/2-\varepsilon}\frac{1-\sin\alpha}{\cos(\alpha)}d\alpha-\cos\varepsilon-\ln(\sin\varepsilon)\,, \tag{A3}$$

while the integral in the right side converges to a constant with $\varepsilon\to 0$, as well as the $\cos\varepsilon$. Numerical calculation gives

$$\int_0^{\pi/2}\frac{1-\sin\alpha}{\cos(\alpha)}d\alpha=0.6931\ . \tag{A4}$$

Therefore, when $\varepsilon\to 0$

$$I(\varepsilon)\approx -0.3068-\ln\varepsilon\ \ . \tag{A5}$$

Integral

$$\int_{(1-n)r-\Delta x/2}^{(1-n)r}\frac{x^2}{r^2-x^2}dx \tag{A6}$$

can be approximately evaluated taking into consideration that its limits are the values very close to unity, and that $nr<<\Delta x$. Therefore, the nominator of the underintegral function can be set approximately to unity, and, changing the variable of integration to $\varepsilon=1-x/r$, (A6) can be transformed to the following final form:

$$\int_{(1-n)r-\Delta x/2}^{(1-n)r}\frac{x^2}{r^2-x^2}dx\approx -r\int_{\Delta x/2r}^{n}\frac{d\varepsilon}{2\varepsilon}=\frac{r}{2}\ln\frac{\Delta x}{2nr}\ . \tag{A7}$$

Figure captions

Fig.1. The scheme of the X-ray refractive radiography.

Fig.2 Generalized angular characteristic of a crystal analyzer.

Fig.3. Generalized scheme of a multilayer mirror analyzer.

Fig.4. The structure of multilayer mirror with resonant absorption.

Fig.5. Graphical representation of the concept for multilayer mirror with resonant absorption.

Fig.6. Analytical solutions for reflected intensity in two cases: (a) θ_1=0.59º, θ_2=0.61º; (b) θ_1=θ_2=0.6º. The curve (c) represents the case when the intensity is the full quadrate. Values of the parameters are: N=10; λ=1.54Å; d=73.5Å; θ_r=0.6º.

Fig.7. Calculated reflection curve for Ni/C multilayer mirror with resonant absorption at 0.8°. N =30; λ =1.54Å; spacer thickness 217Å; interfacial roughness 5Å.

Fig.8. Calculated reflection curve for Ni/C multilayer mirror with resonant absorption at 0.8°. N =30; λ =1.54Å; spacer thickness 2765Å; interfacial roughness 5Å.

Fig.9. System of coordinates in the cross section of a fiber.

Fig.10. Theoretical intensity distribution behind the mirror analyzer. Absorption is not taken into account.

Fig.11. Numerical simulation of the intensity distribution behind the mirror analyzer. Spatial resolution of the detector was chosen to be 10 mkm. CuK_α radiation.

Fig.12. Geometrical scheme of the detection.

Fig.13. Simulated detector signals for a human hair of 50 μm in diameter with different spatial resolution of a detector: (a) Δx=10 μm; (b) Δx=20 μm; (c) Δx=40 μm. CuK_α radiation.

Fig.14. Physical model for numerical simulation.

Fig.15. Computer generated images for different materials of the immersed ball: (a) W; (b) Ca; (c) SiO_2; (d) C; (e) β-keratin. Exposure: 200,000 photons. The wavelength 1.54Å. Left column presents images in plane P_1 ,right one – images in plane P_2 .

Fig.16. Scheme of the deposition technique: 1- flow controller; 2 -pressure gauge.

Fig.17. Reflection curve of the mirror. The angular axis is directed from right to left.

Fig.18. Scheme of "ω-x" mapping.

Fig.19. 2D "ω-x" map of multilayer mirror (a) and its 3D representation (b).

Fig.20. Optical scheme of the experiment.

Fig.21. One-dimensional images of a copper wire of 75 μm in diameter: (a) refraction-contrast mode; (b) absorption mode. The refraction-contrast peaks are marked with arrows.

Fig.22. One-dimensional refraction-contrast images of different human hairs: (a) a hair with low absorption; (b) a hair with high absorption. Absorption dips are marked with arrows.

Fig.23. Dark-field refraction-contrast images of a human hair: (a) probe beam is aligned to the resonant dip; (b) probe beam is slightly misaligned from the resonant dip; (c) absorption contrast image.

Table caption

Table 1. Sharpness v of the resonant dip of Ni/C multilayer mirror for various number of layers, (arc second)$^{-2}$. θ_r =0.6º .

Table 2. Sharpness v of the resonant dip of Ni/C multilayer mirror for various resonant angles, (arc second)$^{-2}$. N=30.

wavelength, Å	number of layers		
	30	50	100
CuK , 1.54Å	$2.05 \cdot 10^{-2}$	$2.99 \cdot 10^{-2}$	$3.47 \cdot 10^{-2}$
MoK , 0.71Å	$7.30 \cdot 10^{-4}$	$3.90 \cdot 10^{-3}$	$1.99 \cdot 10^{-2}$

Table 1.

wavelength, Å	resonant angle			
	0.3º	0.6º	0.9º	1.1º
CuK , 1.54Å	total external reflection	$2.05 \cdot 10^{-2}$	$1.95 \cdot 10^{-3}$	$4.92 \cdot 10^{-4}$
MoK , 0.71Å	$2.56 \cdot 10^{-2}$	$7.30 \cdot 10^{-4}$	$2.08 \cdot 10^{-5}$	$2.18 \cdot 10^{-7}$

Table 2.

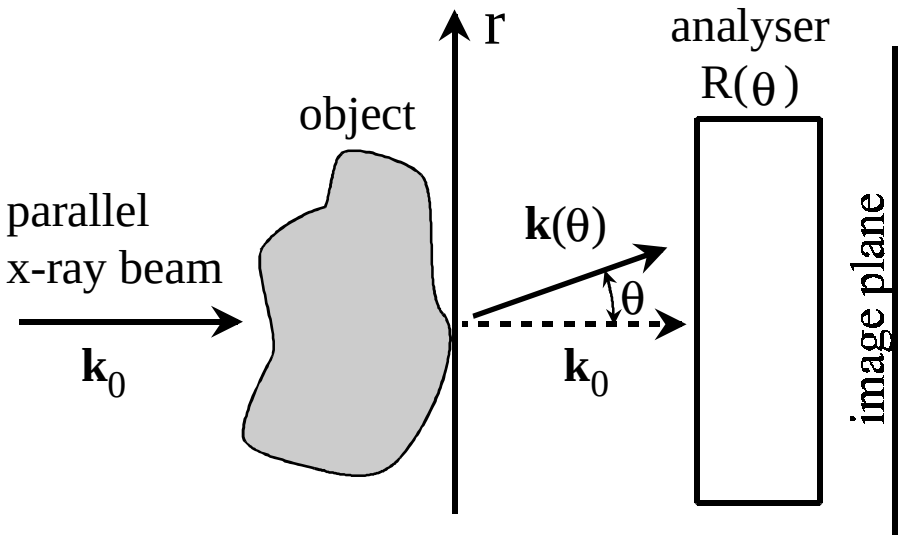
r
analyser
R(θ)
object
parallel
x-ray beam
k(θ)
θ
k0
k0
image plane

Fig.1.

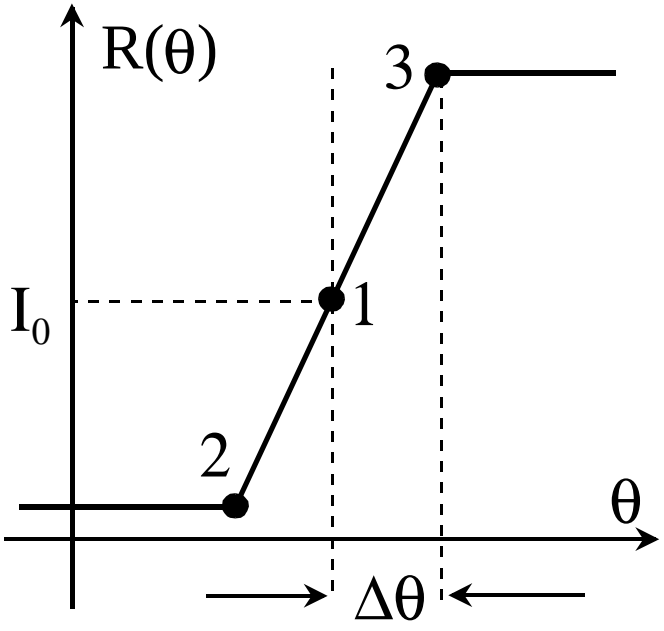

Fig.2.

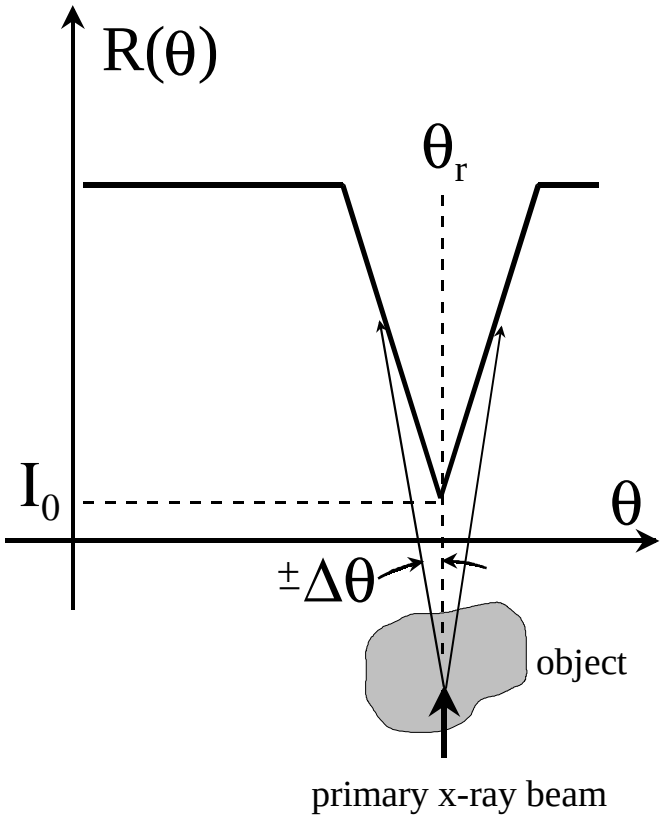

Fig.3.

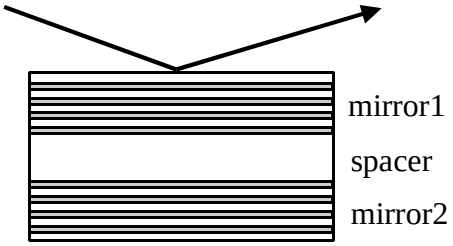

Fig.4.

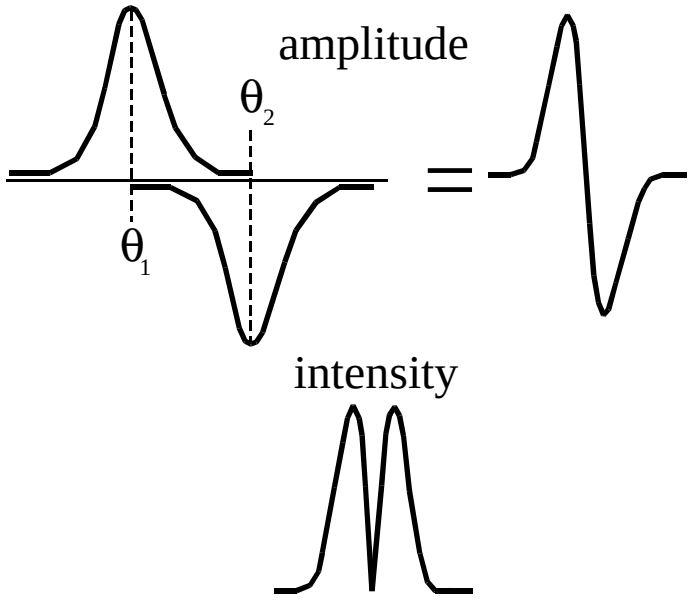

Fig.5

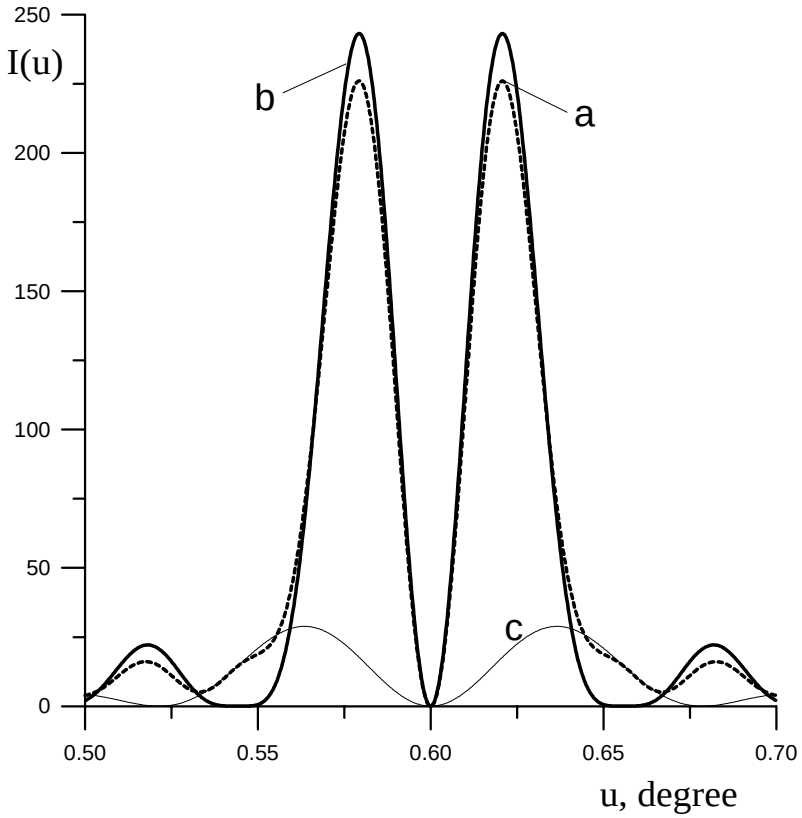

Fig.6

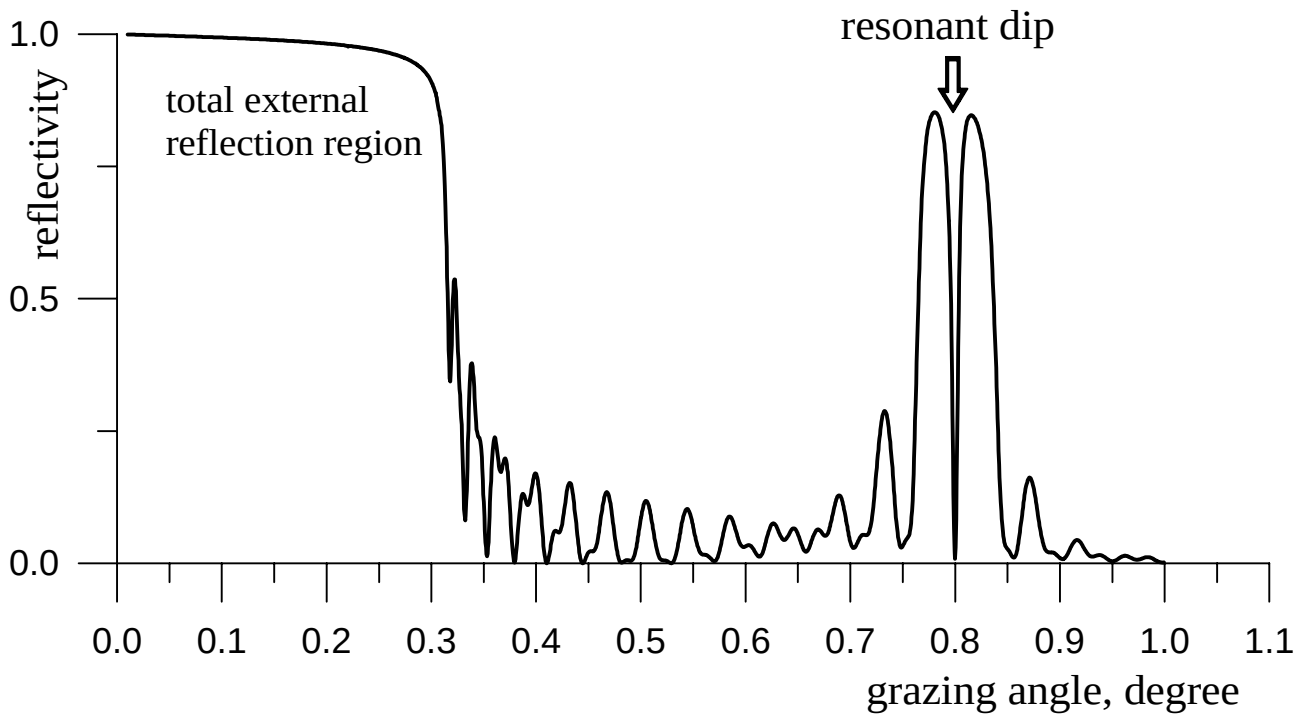
resonant dip
total external
reflection region
reflectivity
1.0
0.5
0.0
0.0
0.1
0.2
0.3
0.4
0.5
0.6
0.7
0.8
0.9
1.0
1.1
grazing angle, degree

Fig.7.

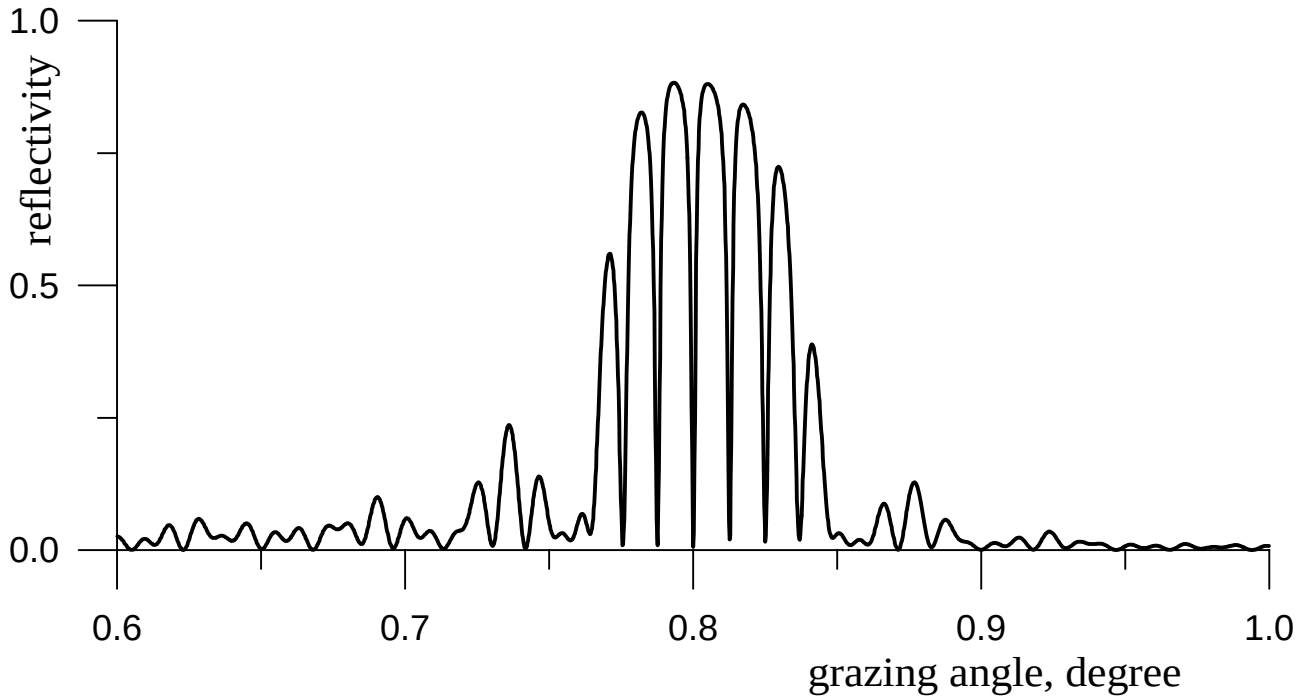

Fig.8

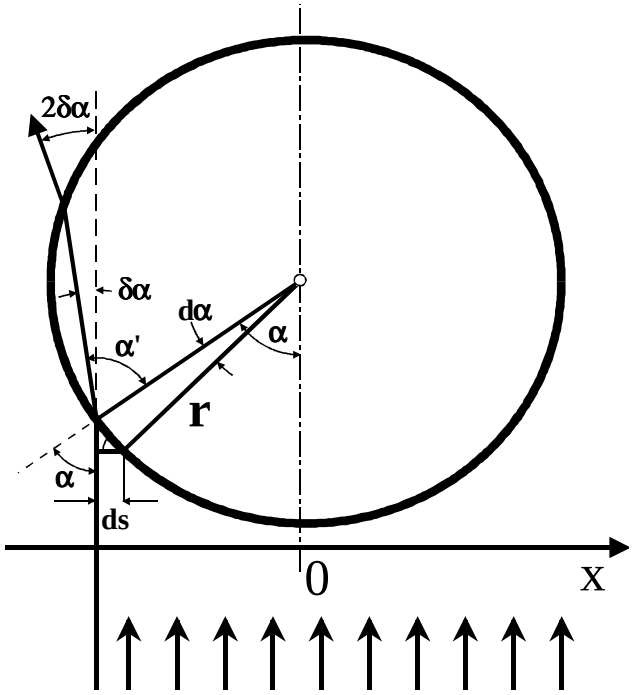

Fig.9

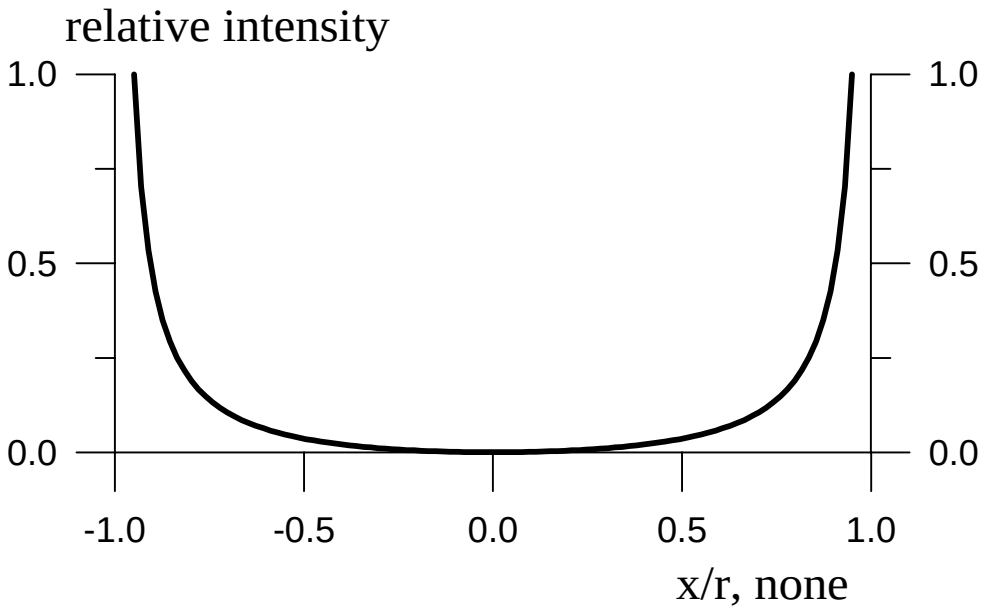

Fig.10

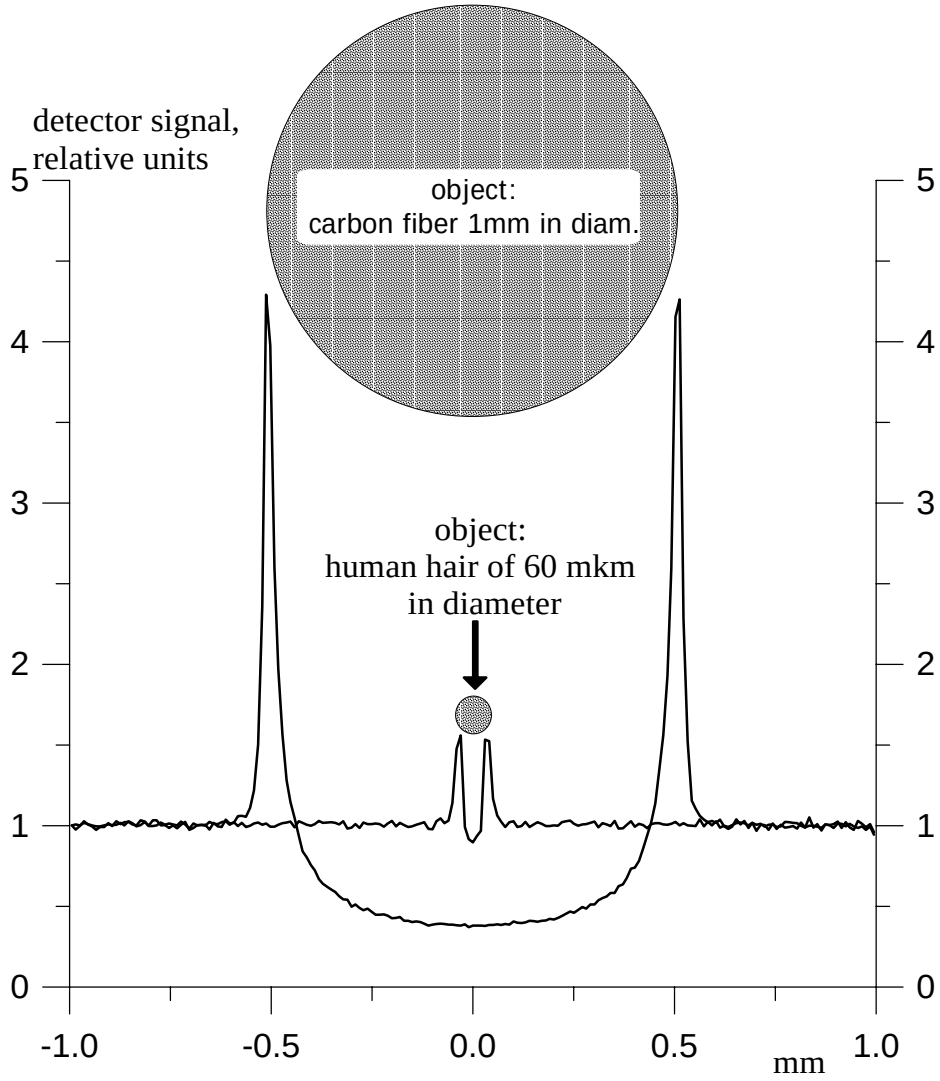
detector signal,
relative units
object:
carbon fiber 1mm in diam.
object:
human hair of 60 mkm
in diameter
5
4
3
2
1
0
-1.0
-0.5
0.0
0.5
1.0
mm

Fig.10

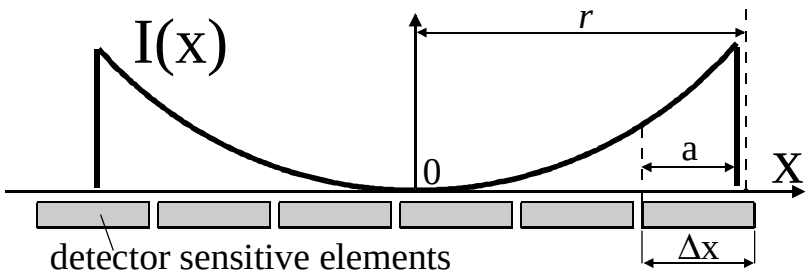

Fig.12

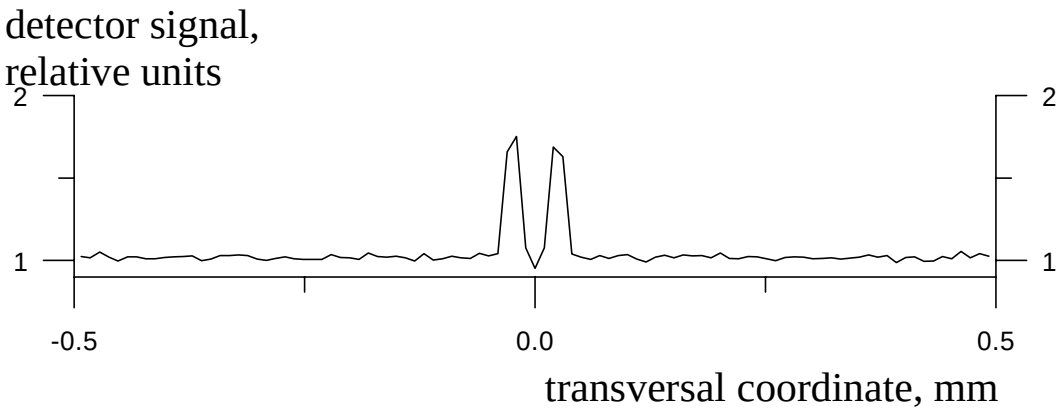
detector signal,
relative units
2
1
2
1
-0.5
0.0
0.5
transversal coordinate, mm

a

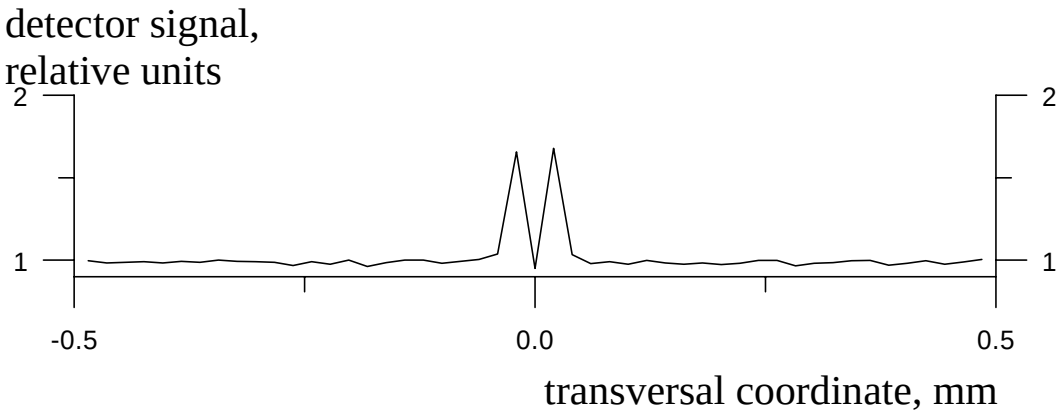
detector signal,
relative units
2
1
2
1
-0.5
0.0
0.5
transversal coordinate, mm

b

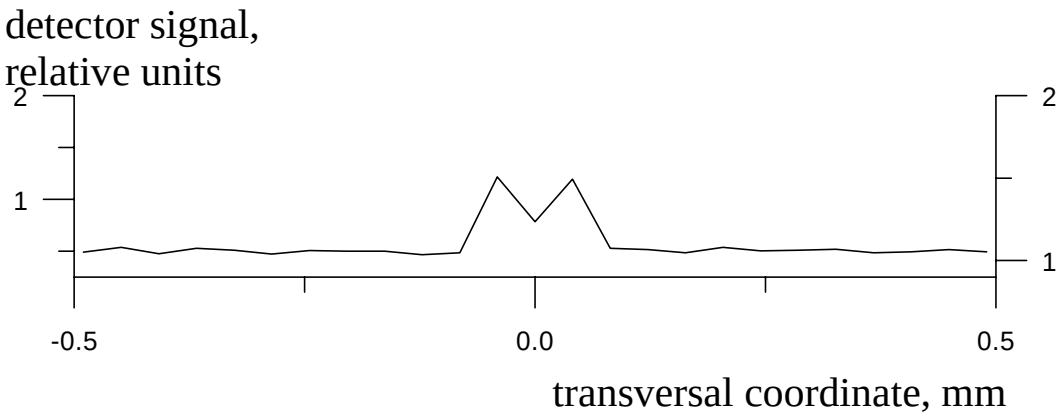
detector signal,
relative units
2
1
2
1
-0.5
0.0
0.5
transversal coordinate, mm

c

Fig.13.

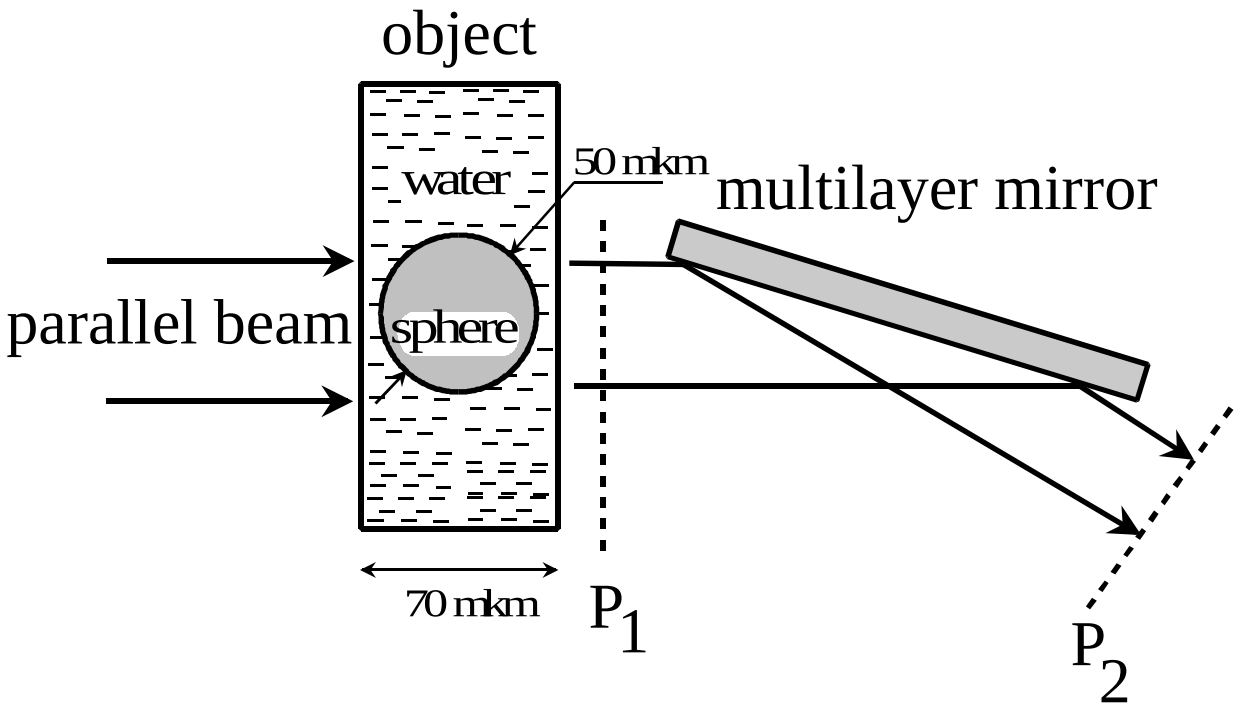
object
water
50 mkm
multilayer mirror
parallel beam
sphere
70 mkm
P1
P2

Fig.14.

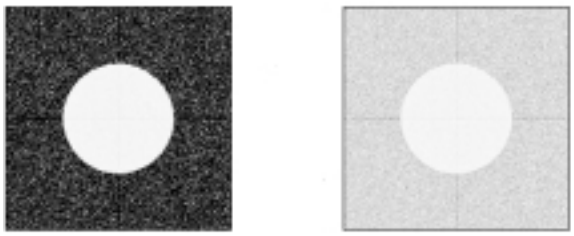

a

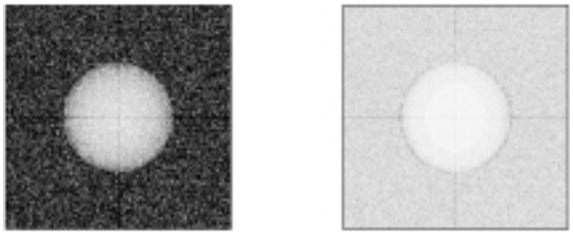

b

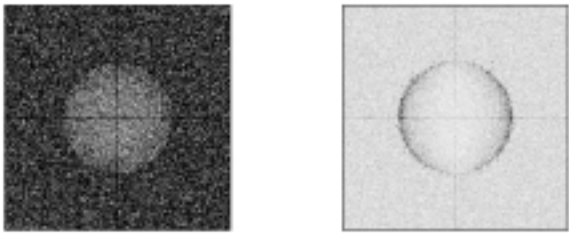

c

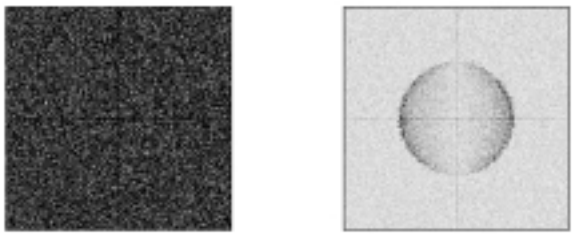

d

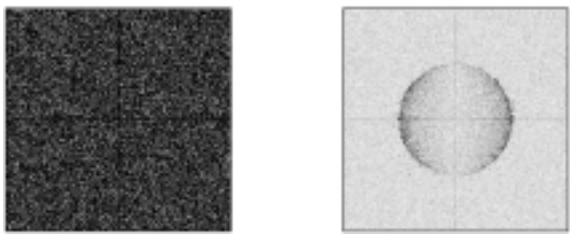

e

Fig.15.

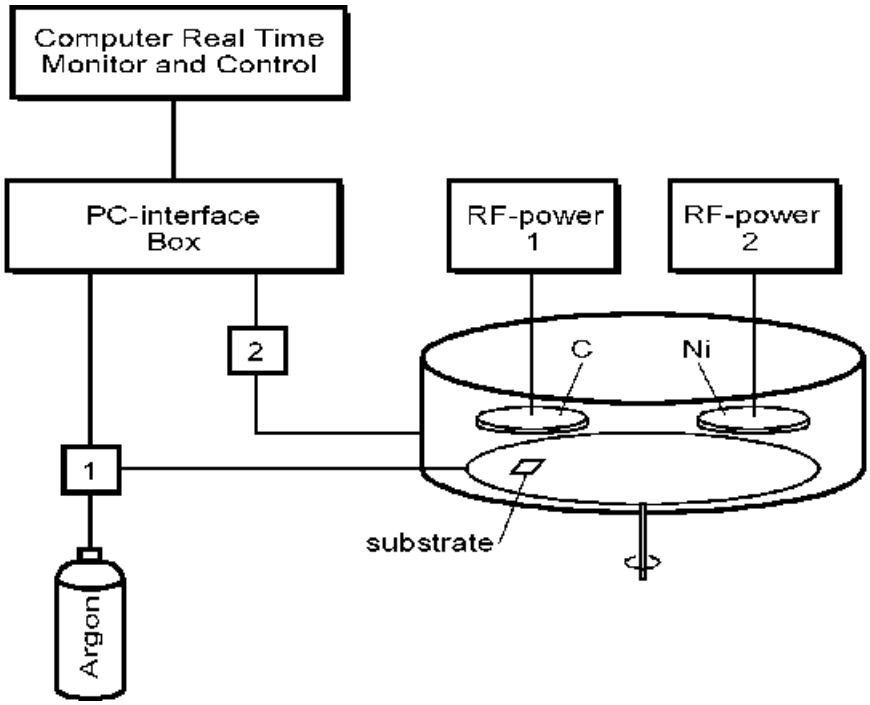
Computer Real Time
Monitor and Control
PC-interface
Box
RF-power
1
RF-power
2
2
C
Ni
1
substrate
Argon

Fig.16.

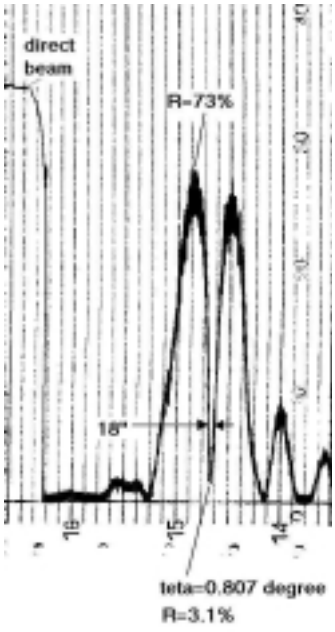

Fig.17.

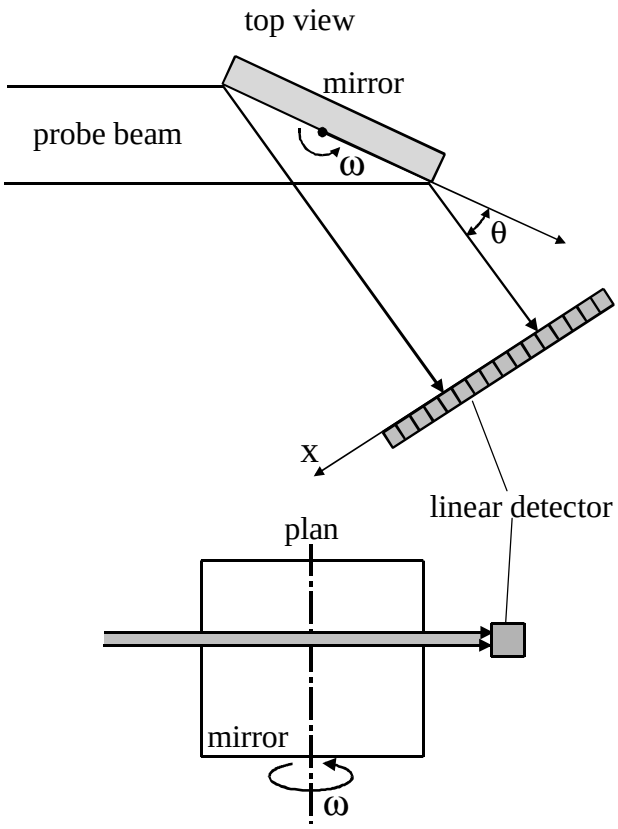
top view
mirror
probe beam
ω
θ
x
linear detector
plan
mirror
ω

Fig.18

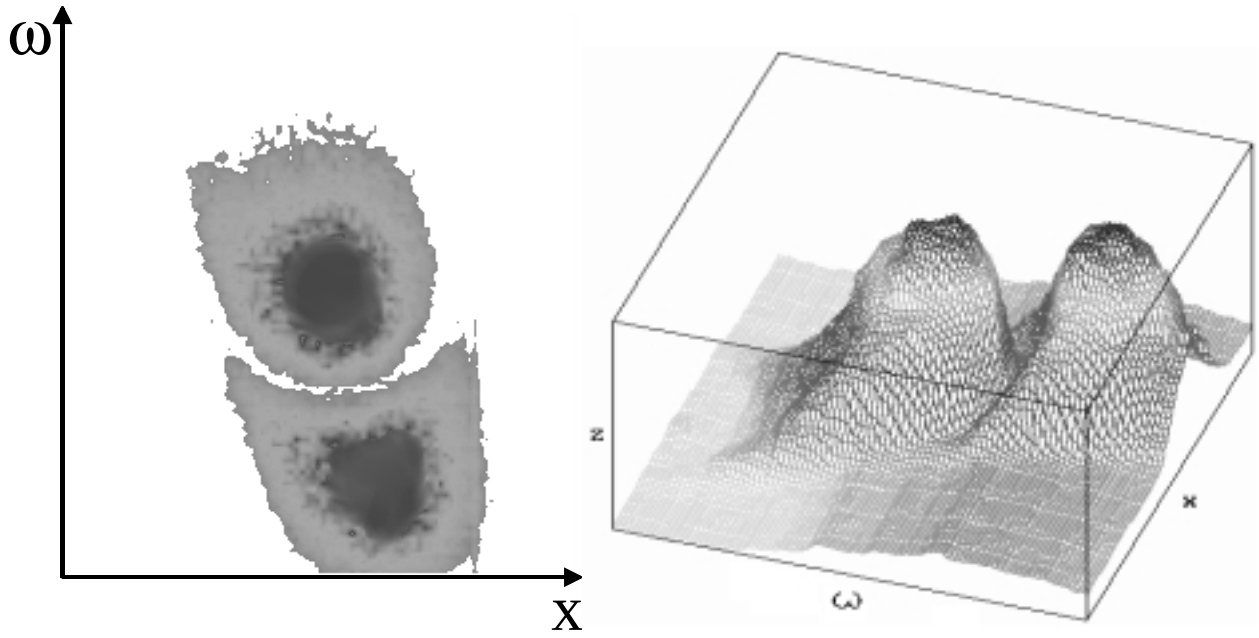

a b

Fig.19

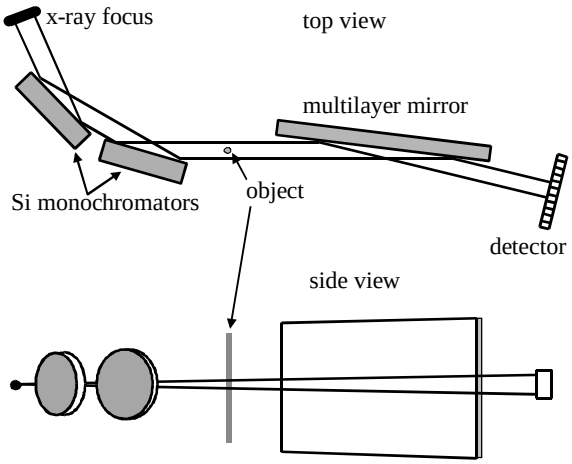
x-ray focus
top view
multilayer mirror
Si monochromators
object
detector
side view

Fig.20.

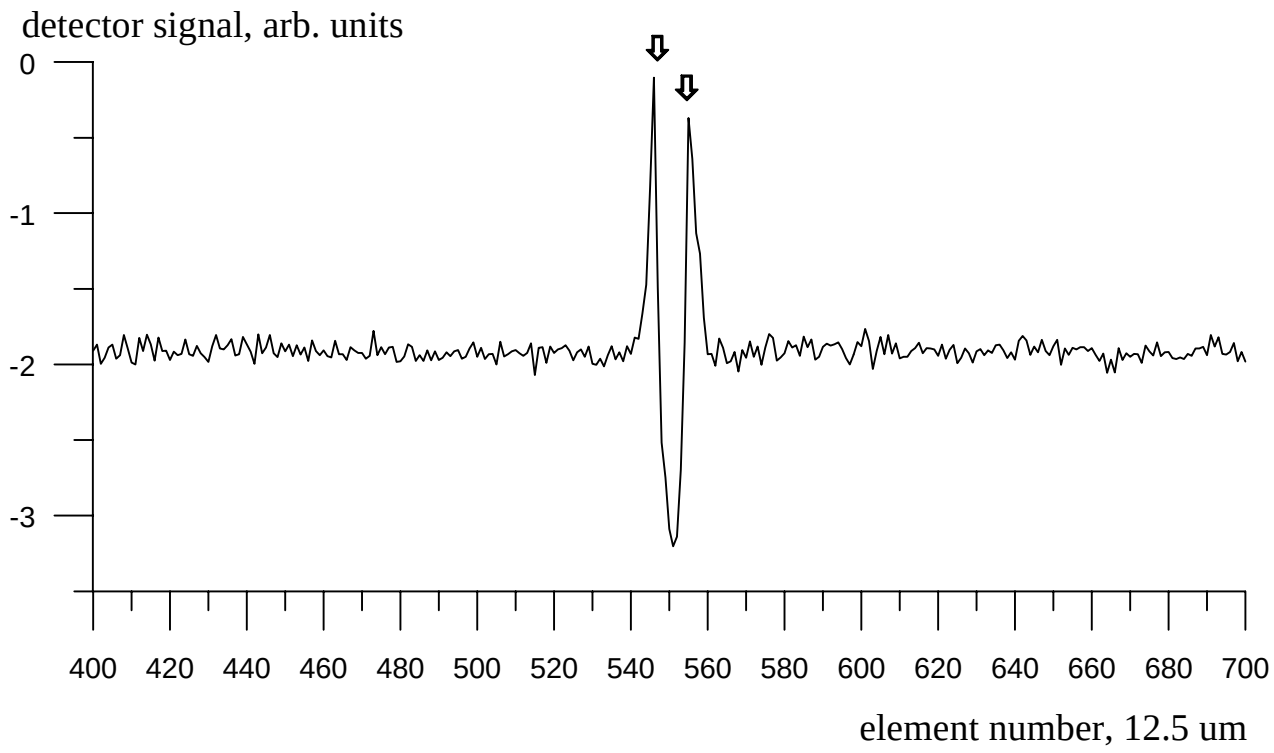
detector signal, arb. units
0
-1
-2
-3
400 420 440 460 480 500 520 540 560 580 600 620 640 660 680 700
element number, 12.5 um

a

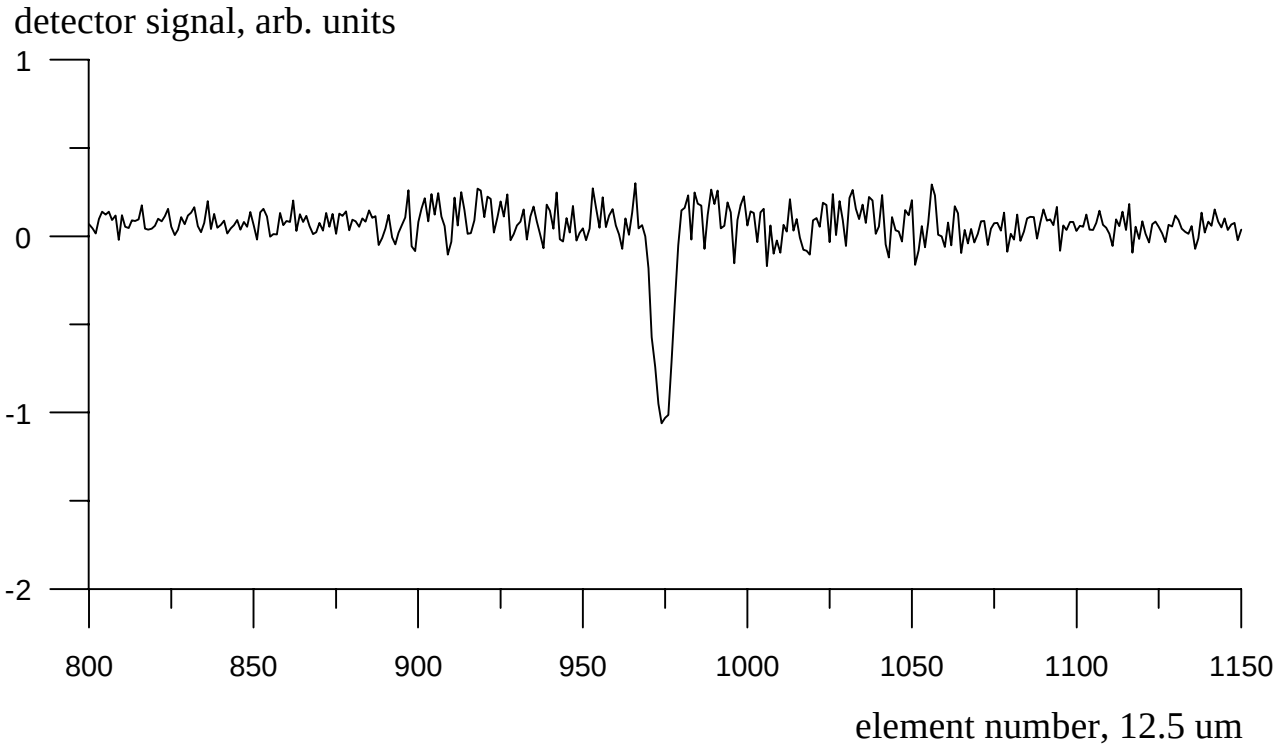
detector signal, arb. units
1
0
-1
-2
800 850 900 950 1000 1050 1100 1150
element number, 12.5 um

b

Fig.21

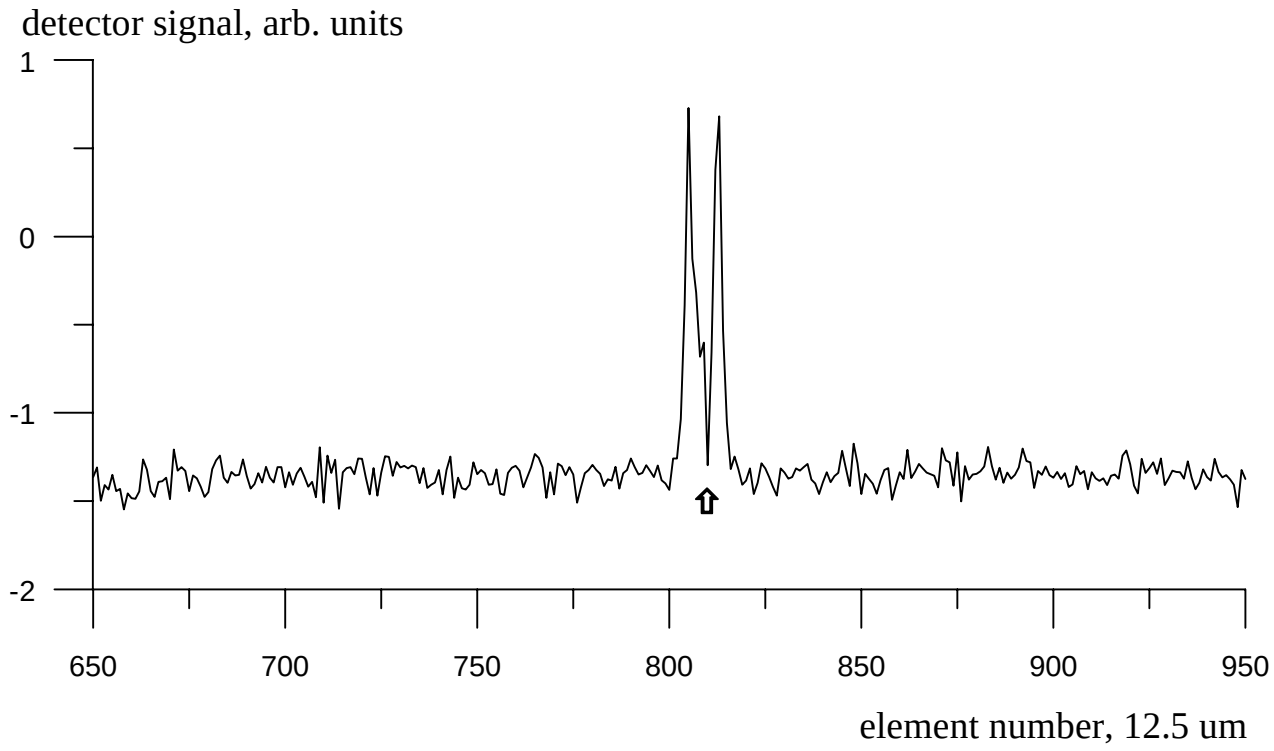
detector signal, arb. units
1
0
-1
-2
650
700
750
800
850
900
950
element number, 12.5 um

a

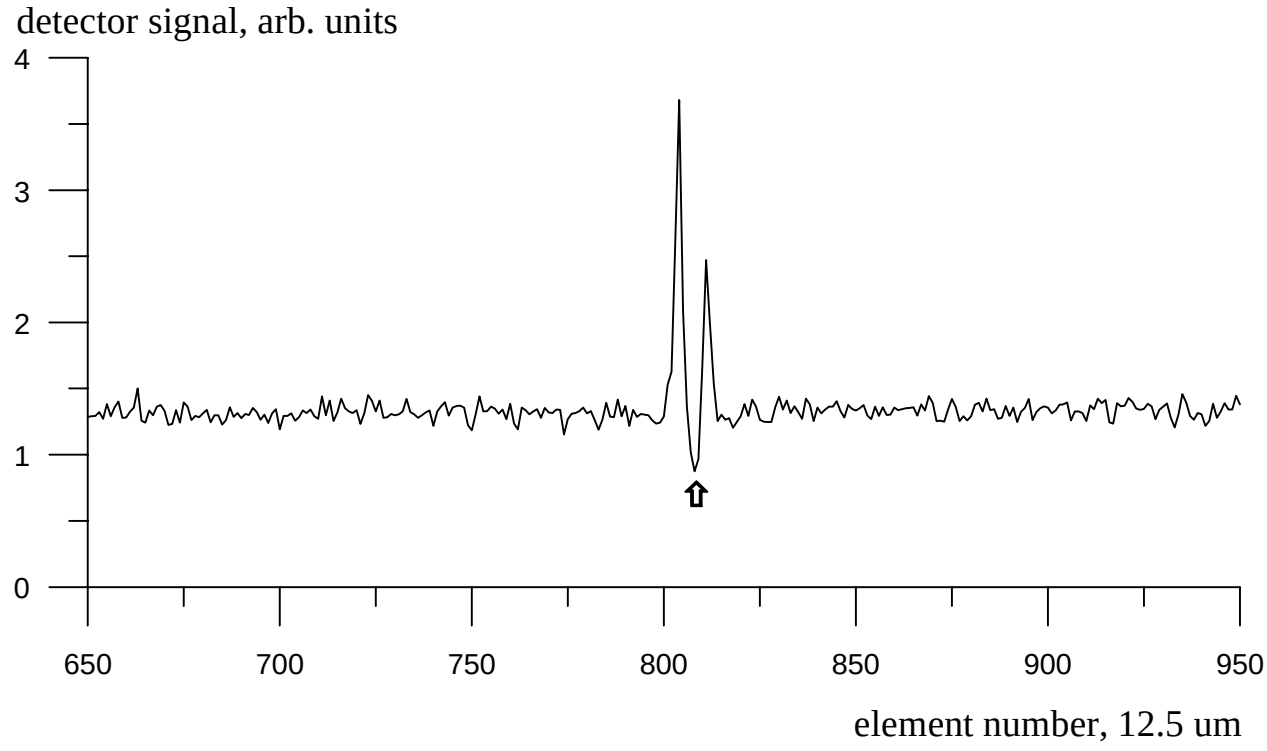
detector signal, arb. units
4
3
2
1
0
650
700
750
800
850
900
950
element number, 12.5 um

b

Fig.22

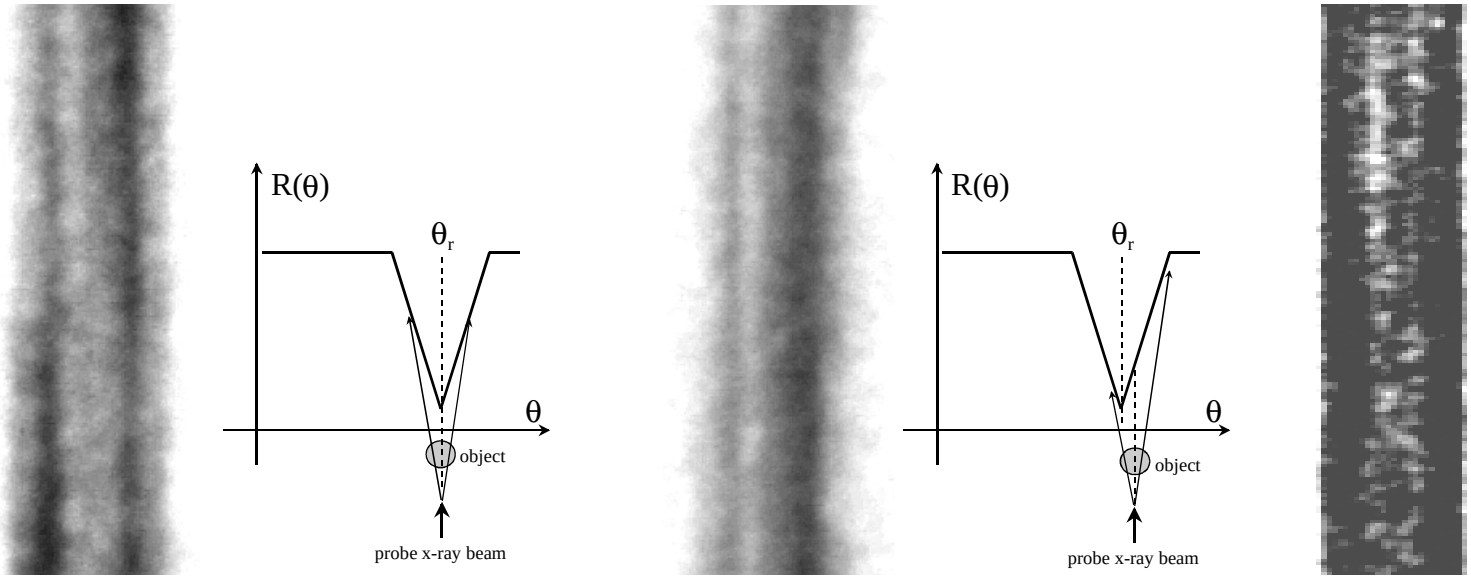

a b c

Fig.23